Journal of Computational Physics 330 (2017) 615–623

Contents lists available at ScienceDirect

Journal of Computational Physics

www.elsevier.com/locate/jcp

Short note

On the eddy-resolving capability of high-order discontinuous Galerkin approaches to implicit LES / under-resolved DNS of Euler turbulence

R.C. Moura *, G. Mengaldo, J. Peiró, S.J. Sherwin

Department of Aeronautics, Imperial College London, SW7 2AZ, United Kingdom

ARTICLE INFO

Article history:
Received 12 May 2016
Received in revised form 4 October 2016
Accepted 25 October 2016
Available online 29 October 2016

Keywords:
Implicit LES
Under-resolved DNS
Dispersion–diffusion analysis
High-order discontinuous Galerkin
Inviscid Taylor–Green vortex
Euler turbulence

ABSTRACT

We present estimates of spectral resolution power for under-resolved turbulent Euler flows obtained with high-order discontinuous Galerkin (DG) methods. The '1% rule' based on linear dispersion–diffusion analysis introduced by Moura et al. (2015) [10] is here adapted for 3D energy spectra and validated through the inviscid Taylor–Green vortex problem. The 1% rule estimates the wavenumber beyond which numerical diffusion induces an artificial dissipation range on measured energy spectra. As the original rule relies on standard upwinding, different Riemann solvers are tested. Very good agreement is found for solvers which treat the different physical waves in a consistent manner. Relatively good agreement is still found for simpler solvers. The latter however displayed spurious features attributed to the inconsistent treatment of different physical waves. It is argued that, in the limit of vanishing viscosity, such features might have a significant impact on robustness and solution quality. The estimates proposed are regarded as useful guidelines for no-model DG-based simulations of free turbulence at very high Reynolds numbers.

1. Introduction

DG (and other discontinuous spectral element) methods have been successfully employed in eddy-resolving computations of turbulence through the so-called implicit LES approach [1–5], where, broadly speaking, numerical errors are expected to play the role of turbulence models. The term implicit LES has however been more traditionally connected to numerical methods whose truncation errors resemble subgrid-scale models of classical LES approaches [6,7]. As this property has not yet been formally demonstrated for DG [8,9], the term under-resolved DNS (uDNS) is here preferred to describe DG-based eddy-resolving simulations without added subgrid models. Linear dispersion–diffusion analysis has suggested that DG's suitability for uDNS is due to its convenient spectral dissipation [10], which does not affect the large scales directly and is only significant at high wavenumbers/frequencies. Still, the suitability of DG-uDNS for general flows at very high Reynolds numbers is not yet fully understood (especially for wall-bounded flows). More research is therefore necessary to assess whether no-model DG (and related) approaches are capable of providing usefully accurate solutions for different types of flows when molecular viscosity is negligible.

One of the fundamental questions regarding uDNS approaches concerns their resolution power or eddy-resolving capability. A natural candidate for the effective grid size of a spectral element setting is $h/(p+1)$, h and p being the mesh spacing

* Corresponding author.
E-mail address: r.moura13@imperial.ac.uk (R.C. Moura).

http://dx.doi.org/10.1016/j.jcp.2016.10.056

and the polynomial order employed. This measure relates to the number of degrees of freedom (DOFs) since $m = p + 1$ is the number of polynomial modes per element (and per dimension). However, for example when DG-based uDNS test cases of the same DOFs are compared, higher-order solutions (on coarser meshes), can outperform low-order ones (on finer grids) and follow much more closely reference DNS results [11]. The effects of h and p in terms of eddy-resolving capability have been further assessed in [10], where a simple criterion was proposed to estimate DG's effective resolution power for under-resolved computations. In [10], this criterion was named 'the 1% rule' and validated against one-dimensional Burgers turbulence. Here, the 1% rule is adapted for three-dimensional energy spectra and tested for the first time in a transitional/turbulent flow obtained through the Euler equations.

Euler (or inviscid) turbulence is often regarded as representative of real (Navier–Stokes) turbulence in the limit of very high Reynolds numbers [12,13]. There are however two conditions for this to hold in any given simulation. First, vorticity has to be introduced via boundary and/or initial conditions, since the Euler equations can not generate vorticity from irrotational flows. Secondly, some artificial mechanism (e.g. numerical viscosity) is required in Euler simulations to ensure the dissipative character maintained by Navier–Stokes turbulence in the limit of vanishing viscosity [14]. For the inviscid Taylor–Green vortex [15] problem considered in the present study, vorticity is prescribed at the initial condition and upwind dissipation is relied upon for the enforcement of the entropy-consistent dissipative behaviour of the flow. We expect that the results discussed here are representative of DG-based uDNS of more general free flows (away from walls) at very high Reynolds numbers. Also, the results here shown for DG might be directly extendable to other discontinuous spectral element methods, in particular to certain variants of the flux reconstruction (FR) scheme, given the well established connections between DG and FR methods [16–18].

2. The 1% rule and its validation

The 1% rule had its origin in linear dispersion–diffusion analyses of the DG scheme [10], which showed that DG is able to resolve wave-like solution components accurately up to a certain wavenumber, beyond which numerical dissipation becomes significant. In this sense, an effective resolution power can be defined from the extent of the wavenumber region where numerical dissipation is negligible. More specifically, the 1% rule yields the wavenumber $k_{1\%}$ at which propagating waves have their amplitude scaled by 0.99 per DOF crossed, regardless of their speed — where the DOF measure is $\hbar = h/(p+1) = h/m$. Although seemingly arbitrary, this value has been tested against one-dimensional Burgers turbulence and proven to be a good measure of propagation accuracy for DG. In particular, this criterion was verified to accurately pinpoint the beginning of the (numerically induced) dissipation range on measured energy spectra. The interested reader is referred to [10] for a detailed discussion.

Table 1
Resolution estimates for standard upwind DG: h-scaled cutoff wavenumber $(kh)_{1\%}$, DOFs per wavelength $2\pi/(k\hbar)_{1\%}$ and normalized Gaussian-like filter width $(\Delta/h)_{1\%}$.

p	m	$(kh)^{1d}_{1\%}$	$2\pi/(k\hbar)^{1d}_{1\%}$	$(\Delta/h)^{1d}_{1\%}$	$(kh)^{3d}_{1\%}$	$2\pi/(k\hbar)^{3d}_{1\%}$	$(\Delta/h)^{3d}_{1\%}$
1	2	1.127	11.150	2.788	1.540	8.163	2.041
2	3	2.616	7.205	1.201	3.574	5.275	0.879
3	4	4.330	5.804	0.726	5.915	4.249	0.531
4	5	6.164	5.097	0.510	8.420	3.731	0.373
5	6	8.071	4.671	0.389	11.025	3.419	0.285
6	7	10.027	4.386	0.313	13.697	3.211	0.229
7	8	12.018	4.183	0.261	16.417	3.062	0.191
8	9	14.035	4.029	0.224	19.172	2.950	0.164

Table 1 provides the values of $(kh)_{1\%}$ given by the 1% rule for different discretization orders, both for 1D and 3D Cartesian settings. The associated number of required DOFs per wavelength, $2\pi/(k\hbar)_{1\%}$, is also provided. The 1D values are the same as given in [10], whereas the 3D ones are derived in the present study (Sec. 4). In addition, Table 1 also provides measures of filter width $\Delta = \pi/k_{1\%}$ of an equivalent Gaussian filter of cutoff wavenumber $k_{1\%}$, see e.g. [19]. We stress however that DG's 'implicit filter' is not exactly Gaussian as it is not isotropic in three dimensions, cf. Sec. 4. The estimates presented are expected to hold for full tensor-product basis functions in either modal or nodal form. In fact, while modal basis has been used in [10], nodal basis is employed in this study. Moreover, the values provided assume consistent integration of non-linear terms, as it seems that some resolution power may be lost otherwise [20]. Finally, we note that the values in Table 1 are based on standard upwinding, see [10], and therefore regarded as a baseline for practical stabilized computations.

In this study, the 1% rule is validated through the Taylor–Green vortex (TGV) flow, introduced in [21] as a model problem for the analysis of transition and turbulence decay. The test case was originally proposed for the incompressible Navier–Stokes equations in a cubic domain with triply-periodic boundary conditions. As in [22], we adopt a modified version of the initial conditions that is suited for compressible flow solvers. In addition, we focus on the inviscid and nearly incompressible TGV flow [15], adopting a Mach number of 0.1. The inviscid problem has been chosen so that the effects of upwind dissipation could be directly assessed, but it also allowed for a comparison of the performance of different Riemann fluxes in the limit of vanishing viscosity. We note that the inviscid TGV flow can be extremely demanding in terms numerical

stability and may allow for the formation of singularities [23–25] if the entropy-consistent dissipative character of the flow is not enforced appropriately. As discussed in Sec. 3, some of the considered discretizations lacked stability/robustness.

The three phases of the TGV flow [26], namely, transition, strong dissipation and nearly-homogeneous decay are shown in Fig. 1. Kolmogorov's $-5/3$ slope is followed at $t \approx 9$, when a peak in overall dissipation is achieved [27]. Estimates for the start of the dissipation range (via $k^{3d}_{1\%}$) are shown as vertical lines, cf. Sec. 4. Two Riemann solvers are compared in Fig. 1, which exhibits clear differences between their behaviour at later flow phases, as discussed in the next section. These (inviscid) results have also been reproduced by including the viscous terms at a Reynolds number of 10^6, but the energy spectra were practically indistinguishable. Only upon closer inspection one could see that the smaller scales were slightly less energetic in the viscous cases, thus supporting the claim that the inviscid solutions obtained are representative of under-resolved simulations conducted at very high Reynolds numbers.

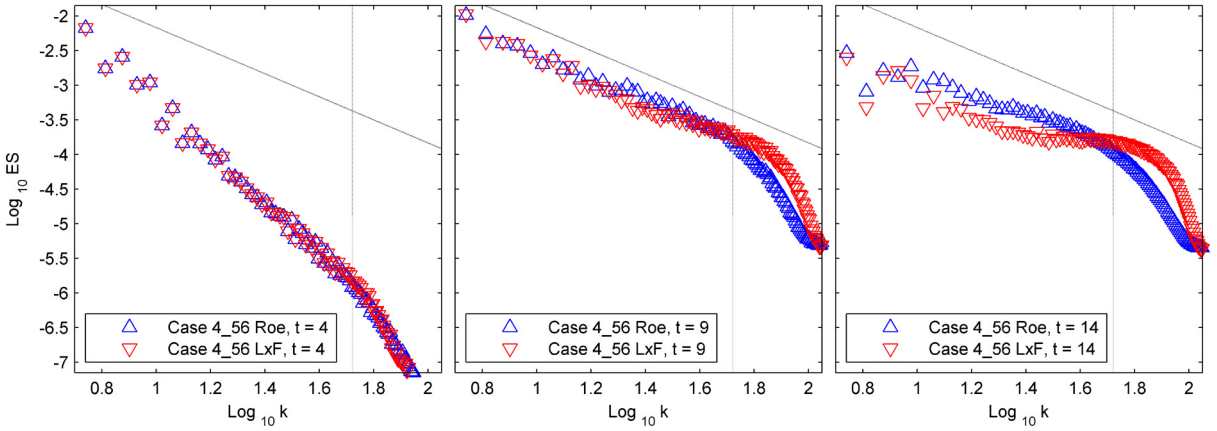

Fig. 1. Three-dimensional energy spectra obtained with Roe (△) and Lax–Friedrichs (▽) at $t = 4$, $t = 9$ and $t = 14$ (left to right). Data obtained from simulations performed with $m = 4$ and $N_{el} = 56^3$. Vertical dashed lines correspond to $k^{3d}_{1\%}$ whereas inclined ones represent the $-5/3$ slope.

3. Test cases and Riemann flux performance

The base set of inviscid test cases considered relied on the Roe and Lax–Friedrichs (Rusanov) solvers, cf. e.g. [28]. This base set is given in Table 2, where each column is associated to a number of polynomial modes $m = p + 1$ and each row represents a given number of DOFs, $N_{dof} = (n_{el}\, m)^3$, which is approximately constant in a row. The number of (cube-shaped) elements per direction is represented by n_{el}, whose values for each test case constitute the body of Table 2. We note that N_{dof} grows by a factor of $2^{3/2}$ between two adjacent rows, corresponding to a factor of $2^{1/2}$ in the number of DOFs per direction ($n_{el}\, m$). Crossed out cases represent unstable simulations which collapsed prior to the third flow phase (nearly-homogeneous decay). Some specific cases have also been carried out with HLL, HLLC and the exact Riemann solver [28]. The energy spectra yielded by each of these solvers practically matched one of the two behaviours shown in Fig. 1. The latter two solvers followed Roe very closely, while the former one yielded results very similar to Lax–Friedrichs, see Fig. 4. This is indicated on the top row of Table 2 and further discussed below. All simulations have been conducted through the spectral/*hp* element code *Nektar*++ [29].

Table 2
Summary of test cases — crossed out numbers indicate cases that crashed.

	Roe (∼ HLLC, Exact)					Lax–Friedrichs (∼ HLL)				
$m = p + 1$	4	5	6	7	8	4	5	6	7	8
n_{el}	28	23	19	16	14	28	23	~~19~~	~~16~~	~~14~~
	39	32	28	23	~~19~~	39	32	~~28~~	~~23~~	~~19~~
	56	45	39	~~32~~	~~28~~	56	45	~~39~~	~~32~~	~~28~~

Table 2 shows that, at least for the problem considered, the Roe solver yields a more robust discretization than Lax–Friedrichs. This is counter-intuitive since Lax–Friedrichs is traditionally regarded as more dissipative (and thus more robust) than Roe. We highlight that such differences are possibly peculiar to high-order DG at extremely high Reynolds numbers. In this limit, different fluxes can exhibit significant differences, see Fig. 1, first at the smallest resolved scales where numerical errors become noticeable (beyond $k_{1\%}$ in particular) and subsequently at larger scales owing to non-linear (triadic) interactions. We note that energy spectrum differences consistent with those found here have also been reported in recent studies involving high-Reynolds DG-based uDNS [30,31].

All the unstable cases provided reasonable results up to the time of crash (without prior signs of instabilities), which consistently took place within the transitional phase of the TGV flow. The lack of robustness for the higher-order discretizations has been cautiously verified not to be related with time-step restrictions or polynomial aliasing errors. Typical CFL

numbers (based on the acoustic wave speed) were of the order of 10^{-1} and an increased number of quadrature points ($q = 2m$ per dimension) has been employed in all the cases to ensure consistent integration of the cubic non-linearities of the compressible Euler equations. Tests conducted with particular cases to rule out these factors consistently showed the time of crash to be insensitive to time-step reductions (down to CFL $\approx 10^{-2}$) or to a further increase in the number of integration points (up to $q = 4m$). The 'global dealiasing' approach described in [32] has been employed for the interior and boundary quadratures, where over-integration is performed simply through a larger number of (Gauss–Lobatto–Legendre) quadrature points. The unstable simulations obtained highlight that DG-based uDNS approaches, even with consistent/over-integration, might in fact require additional stabilization techniques at very high Reynolds numbers so as to more strongly enforce the entropy-consistent dissipative behaviour of Navier–Stokes turbulence in the limit of zero viscosity.

Although the instabilities observed are not entirely understood at this point, one possible explanation stems from the sharper dissipative behaviour (in Fourier space) of higher-order DG discretizations [10]. We believe that a sharp dissipation might induce the energy-conserving character of the inviscid TGV flow to overcome the fully dissipative behaviour expected from LES-like results in the limit of vanishing viscosity. A sharper dissipation is known to induce a stronger bottleneck effect [33,34], promoting a pile-up of energy prior to the dissipation range. DNS experiments using hyperviscosity in place of regular viscosity have demonstrated that such 'energy bumps' grow as the hyperviscous exponent increases [35]. Complementary studies [36,37] showed that energy bumps emerge as the solution begins to follow an energy-conserving dynamics when only a finite number of Fourier modes are retained (consistent with the limit of increasingly sharp dissipation). While following this energy-conserving behaviour, the exact inviscid (Euler-based) evolution of the TGV flow may well develop singularities leading to the actual collapse of the solution, although this is still an open issue [23–25]. We stress that the Lax–Friedrichs flux is expected to yield an even sharper spectral dissipation, see [9], due to its over-upwind bias for the momentum equations, especially at low Mach numbers, owing to the disparity between acoustic and convective speeds.

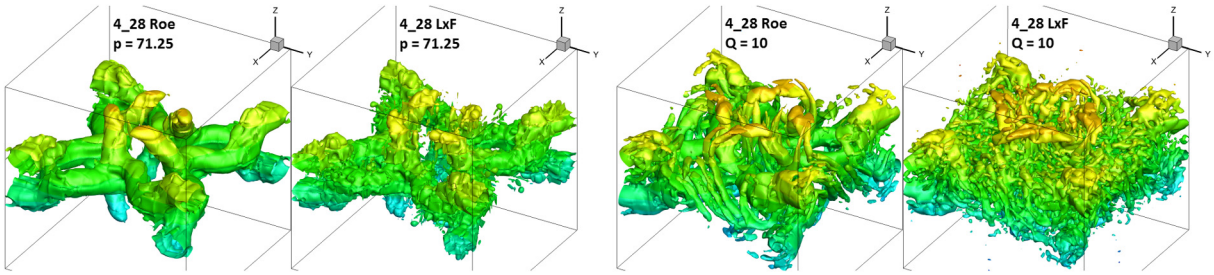

Fig. 2. Isosurfaces of pressure (left pair) and Q-criterion (right pair) comparing simulations based on Roe (cleaner) and Lax–Friedrichs (noisier). Results obtained from test case $m = 4$, $n_{el} = 28$, at $t = 7$. Only one-eighth of the domain is shown; isosurfaces coloured by height (z-coordinate).

A complete assessment of solution quality is difficult since a DNS solution is simply out of reach for the inviscid TGV flow. Nevertheless, the energy spectra in Fig. 1 clearly show that the Lax–Friedrichs flux allows for an excessive accumulation of energy at the smallest captured scales, invariably connected to small non-physical structures highly contaminated by numerical errors (e.g. dispersion). This is illustrated in Fig. 2, where eddies of Roe-based computations are shown to be cleaner and better defined when compared to those obtained with Lax–Friedrichs. These eddies are visualized either via isosurfaces of pressure or by the Q-criterion [38]. Another feature observed at later times in the spectra of Fig. 1 is that the intermediate scales of Lax–Friedrichs computations are less energetic. We believe this results from a spurious energy drain caused by the over-energetic small scales through an intense eddy viscosity-like mixing effect (as discussed in [36,39]). On the other hand, Roe-based simulations yielded spectra which, at the nearly-homogeneous decay phase, look very similar to those obtained via classical LES approaches for homogeneous isotropic turbulence at infinite Reynolds number [40]. In addition, near the dissipation peak, Roe-based spectra follow Kolmogorov's $-5/3$ law over a larger wavenumber range, see also Fig. 4. Although a complete assessment of solution quality has not been made, the results discussed do not encourage the use of more simplistic Riemann solvers (such as HLL and Lax–Friedrichs) in DG-based uDNS, especially at high Reynolds and low Mach numbers.

4. One-dimensional and three-dimensional energy spectra

The energy spectra here considered are based on equispaced grids of $(n_{el}\, m)^3$ points, so that the number of Fourier modes extracted from a given case is consistent with its DOFs. The points inside each element are centred in order to avoid probing data at elemental interfaces. For example, element $[0, h]^3$ contains the set of points defined by the (triple) Cartesian product of coordinates $(j - 1/2)\, h/m$, for $j = 1, \ldots, m$. The grid points in the remaining elements are defined analogously. From this grid, a discrete 3D Fourier transform can directly provide the standard 'three-dimensional energy spectrum'. We recall that the standard spectrum represents the density of kinetic energy in spectral space as distributed over spherical shells of radius $k = (\kappa_x^2 + \kappa_y^2 + \kappa_z^2)^{1/2}$, where κ_η is the wavevector component along axis η. Alternatively, a 'one-dimensional energy spectrum' can be defined as follows. A discrete 1D Fourier transform can be applied over each set of $(n_{el}\, m)$ points aligned with direction η to provide a single 1D energy spectrum. If an average is performed with all

the $(n_{el}\,m)^2$ single 1D energy spectra aligned with η, one ends up with an averaged 1D energy spectrum for this direction. Finally, if averaged 1D spectra are obtained for the two remaining directions and averaged again, a 'one-dimensional energy spectrum' of the TGV flow is obtained. This spectrum is shown in the Appendix to represent the distribution of energy over cubic surfaces in Fourier space, where $k = |\kappa_x| = |\kappa_y| = |\kappa_z|$.

Since the 1% rule was originally devised for 1D settings [10], the validation tests regarding its application to the TGV flow initially considered the one-dimensional energy spectrum defined above. These tests showed that the values of $k^{1d}_{1\%}$ accurately pinpoint the beginning of the dissipation range for all the test cases addressed. The left plot in Fig. 3 compares (compensated) one-dimensional energy spectra at peak dissipation against the respective values of $k^{1d}_{1\%}$ for Roe-based cases with same DOFs and different polynomial orders (first row of cases in Table 2). We note that the horizontal axes in Fig. 3 have been normalized by the grid's Nyquist wavenumber $k_{NY} = \pi m/h$, which is approximately constant for the cases shown. The considered (left-hand side) plot indicates that, in Fourier space, dissipation is only significant outside the region $|\kappa_x| = |\kappa_y| = |\kappa_z| < k^{1d}_{1\%}$ and that DG's iso-dissipation surfaces seem to be cube-shaped (or nearly so) in Fourier space. This behaviour is however likely to depend on the mesh topology. These results have also been verified to be consistent with DG's dissipation characteristics for the wave equation in two dimensions [41], in that, at a given (large) wavenumber k, waves aligned with the (Cartesian) mesh suffer more dissipation than 'diagonal' waves.

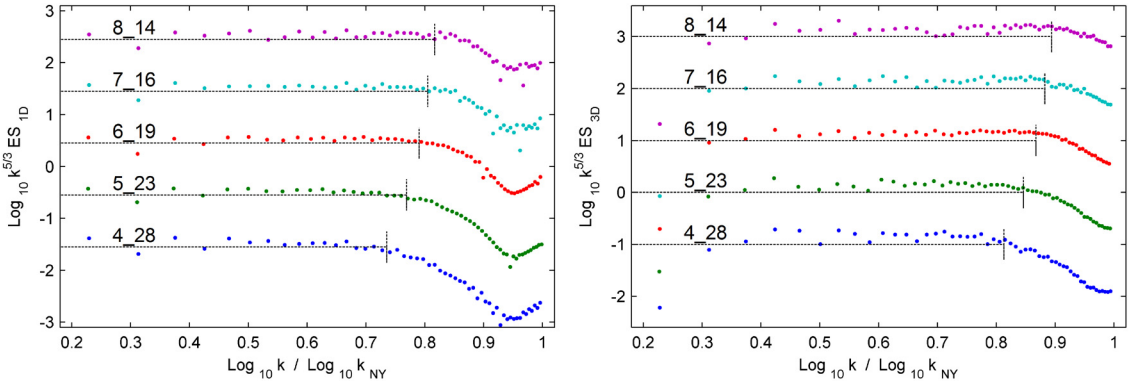

Fig. 3. Compensated one-dimensional (left) and three-dimensional (right) energy spectra at $t = 9$ from Roe-based cases with same DOFs and different polynomial orders ($m = 4, \ldots, 8$). 1% rule estimates (1D and adapted 3D versions) mark the beginning of the dissipation range for each case. Curves have been shifted vertically for clarity, from bottom to top. The notation m_n_{el} is used in the plots to differentiate between test cases.

The one-dimensional spectra previously obtained allow us to anticipate the shape of standard three-dimensional spectra as follows. When the radius k of the spherical shell in Fourier space is $k \gtrsim k^{1d}_{1\%}$, some of the surface wavevectors will begin to suffer dissipation, but the majority of them will still be within the dissipation-free cubic region delimited by $|\kappa_x| = |\kappa_y| = |\kappa_z| = k^{1d}_{1\%}$. In fact, it is not until $k \gtrsim \sqrt{3}\,k^{1d}_{1\%}$ that all the surface wavevectors will perceive significant dissipation, as the shell's diameter begins to surpass the diagonal of the dissipation-free cube. Hence, in practice, the dissipation zone of three-dimensional spectra should start somewhere between $k^{1d}_{1\%}$ and $\sqrt{3}\,k^{1d}_{1\%}$. This was indeed verified to be true for all the test cases addressed. For simplicity, the 1% rule threshold for three-dimensional spectra is defined as the averaged estimate $k^{3d}_{1\%} = \frac{1}{2}(\sqrt{3}+1)\,k^{1d}_{1\%}$, whose values are those given in Table 2. The right-hand side plot of Fig. 3 shows how good this averaged estimate is for three-dimensional spectra of Roe-based computations.

An assessment of the 1% rule for different Riemann solvers is shown in Fig. 4, which compares Roe, HLLC and the exact solver (left plot) against HLL and Lax–Friedrichs (right plot). Fig. 4 shows three-dimensional spectra obtained with $m = 5$, $n_{el} = 23$, at $t = 9$ and $t = 18$. Within each of the two graphs, different fluxes provide practically the same spectra. It is clear from the plots that dissipation begins to take place in between $k^{1d}_{1\%}$ and $\sqrt{3}\,k^{1d}_{1\%}$. Although the fluxes on the right-hand side graph seem to favour the latter threshold, we remark that the presence of the energy bump can somewhat conceal the position where dissipation effectively begins in wavenumber space, see also Fig. 1. Overall, the averaged estimate proposed seems a good choice regardless of the flux employed. We stress that these estimates should only be used in connection to three-dimensional energy spectra, and that $k^{1d}_{1\%}$ is expected to be valid for 1D transforms even in 3D settings, e.g. in spanwise or streamwise spectra of turbulent channel flows. The actual dissipation threshold should however be sensitive to mesh topology as suggested in e.g. [42] and, strictly speaking, the values in Table 1 have only been tested in Cartesian hexahedral meshes. The application of the 1% rule to transitional and turbulent flows in complex geometries and general types of elements has yet to be addressed.

Finally, for finite Reynolds-number flows, the dissipation range of the energy spectrum might begin before $k_{1\%}$ owing to the presence of molecular viscosity. Nevertheless, the 1% rule is still expected to mark the beginning of the numerically induced dissipation range. While in classic LES approaches an explicit subgrid-scale model begins to act (ideally) on scales smaller than the filter width, DG's upwind dissipation in uDNS induces a truncation in the energy cascade beyond $k_{1\%}$. It is hoped therefore that the concept of eddy-resolving capability or resolution power as defined by the 1% rule can be regarded as an effective measure of filter width for more general DG-based uDNS. This work also highlighted the need for stabilization

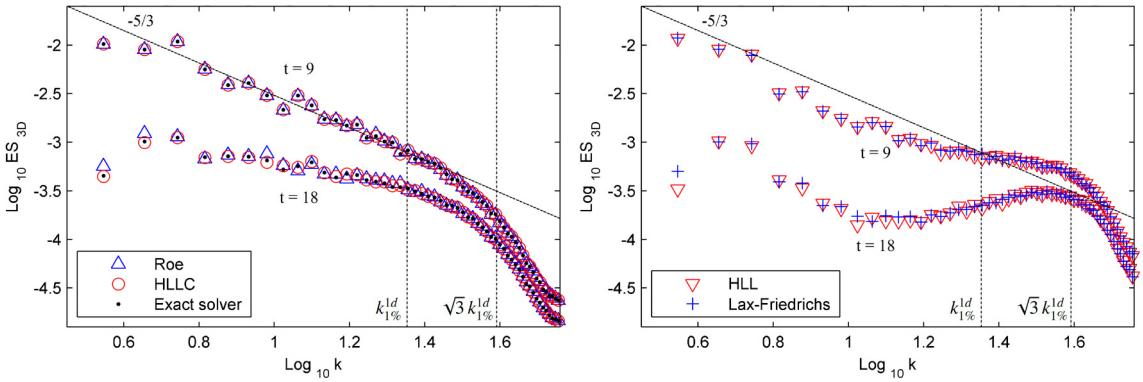

Fig. 4. Three-dimensional energy spectra at $t = 9$ and $t = 18$ yielded by Roe, HLLC and the exact Riemman solver (left) and by HLL and Lax–Friedrichs (right), from case $m = 5$, $n_{el} = 23$. The vertical dashed lines represent, from left to right, $k_{1\%}$ and $\sqrt{3}k_{1\%}$.

techniques to improve DG's robustness while helping to enforce the entropy-consistent dissipative behaviour of turbulent flows at very high Reynolds numbers. Spectral vanishing viscosity (SVV), see e.g. [43,44], might be a viable strategy as it can be tuned to introduce viscous dissipation without compromising DG's effective resolution significantly [45]. Skew-symmetric (or split form) discretizations [46,47] are also worth pursuing as they can improve robustness while preserving the correct evolution of certain flow properties, entropy in particular.

Acknowledgements

RCM would like to acknowledge funding under the Brazilian Science without Borders scheme. GM, JP and SJS would like to acknowledge support from the LFC-UK Centre funded by Airbus/EADS and EPSRC under grants EP/I037946 and EP/L000407. SJS additionally acknowledges support as Royal Academy of Engineering Research Chair under grant 10145/86. Use of the HPC facilities at Imperial College London is also acknowledged.

Appendix

Any quantity $Q(x, y, z)$ in the triply-periodic TGV box $\Omega = [-\pi, \pi]^3$ can be represented through a Fourier expansion as

$$Q(x, y, z) = \sum_{p,q,r} \widehat{Q}_{p,q,r} \exp[i(px + qy + rz)], \tag{1}$$

where $Q \in \mathbb{R} \Leftrightarrow \widehat{Q}_{-p,-q,-r} = \widetilde{Q}_{p,q,r}$, and $\widetilde{Q}_{p,q,r}$ is the complex conjugate of $\widehat{Q}_{p,q,r}$. The Fourier components $\widehat{Q}_{p,q,r}$ can be obtained from a single 3D discrete Fourier transform based on the equispaced grid of $(n_{el}\, m)^3$ points described in the beginning of Sec. 4. We advocate that using m^3 points per element for the transforms is the correct way to probe DG's piecewise continuous numerical fields, as this sets a Nyquist wavenumber $k_{\mathrm{NY}} = \pi m/h$ consistent with the DOFs used in the simulations. Employing more than m^3 points per element is not advisable as Fourier transforms would eventually perceive interface discontinuities and feed on the energy spectra a k^{-2} signature typical of step functions.

Since the volume-averaged energy of variable Q can be expressed as

$$E_Q = \frac{1}{|\Omega|} \int_{\Omega} Q^2 \, d\Omega = \sum_{p,q,r} |\widehat{Q}_{p,q,r}|^2, \tag{2}$$

where $|\widehat{Q}_{p,q,r}|^2 = \widehat{Q}_{p,q,r}\, \widetilde{Q}_{p,q,r}$ and $|\Omega| = (2\pi)^3$, the standard energy spectrum function is given by

$$\mathrm{ES}_Q^{3\mathrm{d}}(k) = \frac{1}{\Delta k} \sum_{S(k)} |\widehat{Q}_{p,q,r}|^2, \tag{3}$$

in which $S(k)$ represents the set of Fourier components within the spherical shell of radius k and thickness Δk such that $k - \Delta k/2 < \sqrt{p^2 + q^2 + r^2} < k + \Delta k/2$. The (volume-averaged) kinetic energy of the TGV flow is defined from Eq. (2) as $K = (E_u + E_v + E_w)/2$, whose spectrum can be obtained by probing the velocity fields independently since

$$\mathrm{ES}_K^{3\mathrm{d}} = \frac{1}{2}\left(\mathrm{ES}_u^{3\mathrm{d}} + \mathrm{ES}_v^{3\mathrm{d}} + \mathrm{ES}_w^{3\mathrm{d}}\right). \tag{4}$$

We stress that Eq. (4) corresponds to the standard three-dimensional energy spectrum, which represents the density of kinetic energy in wavenumber space and whose integral over the range $k \geq 0$ returns the (volume-averaged) kinetic energy

of the flow [19]. In what follows, we show that the 'averaged one-dimensional energy spectrum' defined in Sec. 4 can be understood as an alternative spectrum, where energy is distributed over cubic shells in Fourier space.

We start by considering the one-dimensional spectrum aligned with the z direction and averaged in the x–y plane. By probing the TGV flow field at a set of points equispaced in the z direction with fixed X and Y coordinates, one can write

$$Q(X,Y,z) = \sum_r \widehat{Q}_r(X,Y)\exp(irz)\,, \tag{5}$$

whose coefficients $\widehat{Q}_r(X,Y)$ are obtained from a 1D Fourier transform. These coefficients can be related to the ones of the complete 3D Fourier transform by comparing Eq. (5) with Eq. (1) evaluated at $x = X$ and $y = Y$, which yields

$$\widehat{Q}_r(x,y) = \sum_{p,q} \widehat{Q}_{p,q,r}\,\exp[i(px+qy)]\,. \tag{6}$$

By expressing the averaging operation performed to obtain the averaged one-dimensional spectrum for the z direction as an integration over the x–y plane (confined to Ω), one has

$$Z\text{-}\mathrm{ES}_Q^{1\mathrm{d}}(k) = \frac{1}{(2\pi)^2}\int_{-\pi}^{+\pi}\int_{-\pi}^{+\pi}\frac{1}{\Delta k}\sum_{L(k)}|\widehat{Q}_r(x,y)|^2\,dx\,dy\,, \tag{7}$$

where, for a one-dimensional spectrum, the relevant set $L(k)$ of Fourier components is simply formed by the wavenumbers r such that $k-\Delta k/2 < |r| < k+\Delta k/2$. Now using Eq. (6), we can write

$$|\widehat{Q}_r(x,y)|^2 = \widehat{Q}_r(x,y)\,\widetilde{Q}_r(x,y) = \left[\sum_{p,q}\widehat{Q}_{p,q,r}\,e^{i(px+qy)}\right]\left[\sum_{m,n}\widehat{Q}_{-m,-n,-r}\,e^{-i(mx+ny)}\right]\,, \tag{8}$$

whose last term can have the signs of m and n inverted due to the symmetry of the summation (with respect to $m=n=0$), allowing us to write

$$\int_{-\pi}^{+\pi}\int_{-\pi}^{+\pi}|\widehat{Q}_r(x,y)|^2\,dx\,dy = \sum_{p,q,m,n}\widehat{Q}_{p,q,r}\,\widehat{Q}_{m,n,-r}\int_{-\pi}^{+\pi}e^{i(p+m)x}\,dx\int_{-\pi}^{+\pi}e^{i(q+n)y}\,dy\,, \tag{9}$$

which, since $\int_{-\pi}^{+\pi}\exp[i(p+m)x]\,dx$ equals 2π when $m=-p$ and zero otherwise, becomes

$$\int_{-\pi}^{+\pi}\int_{-\pi}^{+\pi}|\widehat{Q}_r(x,y)|^2\,dx\,dy = (2\pi)^2\sum_{p,q}\widehat{Q}_{p,q,r}\,\widehat{Q}_{-p,-q,-r} = (2\pi)^2\sum_{p,q}|\widehat{Q}_{p,q,r}|^2\,, \tag{10}$$

finally leading to

$$Z\text{-}\mathrm{ES}_Q^{1\mathrm{d}}(k) = \frac{1}{\Delta k}\sum_{L(k)}\sum_{p,q}|\widehat{Q}_{p,q,r}|^2\,. \tag{11}$$

This can be interpreted as a summation over the set of Fourier components distributed within the two planar shells of thickness Δk which are parallel to the p–q plane and centred at $r=\pm k$.

At last, averaging the contributions of each direction yields the 'averaged one-dimensional energy spectrum' of Q as

$$\mathrm{ES}_Q^{1\mathrm{d}} = \frac{1}{3}\left(Z\text{-}\mathrm{ES}_Q^{1\mathrm{d}} + Y\text{-}\mathrm{ES}_Q^{1\mathrm{d}} + Z\text{-}\mathrm{ES}_Q^{1\mathrm{d}}\right)\,, \tag{12}$$

which, by taking into account the three pairs of planar shells associated to each direction, approximately represents the distribution of energy over the cubic shell of thickness Δk supported by $|p|=|q|=|r|=k$. For the kinetic energy, the averaged one-dimensional spectrum can be obtained directly from the averaged one-dimensional spectra of the velocity fields via Eq. (12), so that

$$\mathrm{ES}_K^{1\mathrm{d}} = \frac{1}{2}\left(\mathrm{ES}_u^{1\mathrm{d}} + \mathrm{ES}_v^{1\mathrm{d}} + \mathrm{ES}_w^{1\mathrm{d}}\right)\,. \tag{13}$$

References

[1] M. Parsani, G. Ghorbaniasl, C. Lacor, E. Turkel, An implicit high-order spectral difference approach for large eddy simulation, J. Comput. Phys. 229 (14) (2010) 5373–5393.
[2] A. Uranga, P.O. Persson, M. Drela, J. Peraire, Implicit large eddy simulation of transition to turbulence at low Reynolds numbers using a discontinuous Galerkin method, Int. J. Numer. Methods Eng. 87 (1–5) (2011) 232–261.
[3] A.D. Beck, T. Bolemann, D. Flad, H. Frank, G.J. Gassner, F. Hindenlang, C.D. Munz, High-order discontinuous Galerkin spectral element methods for transitional and turbulent flow simulations, Int. J. Numer. Methods Fluids 76 (8) (2014) 522–548.
[4] J.R. Bull, A. Jameson, Simulation of the Taylor–Green vortex using high-order flux reconstruction schemes, AIAA J. 53 (9) (2015) 2750–2761.
[5] B.C. Vermeire, S. Nadarajah, P.G. Tucker, Implicit large eddy simulation using the high-order correction procedure via reconstruction scheme, Int. J. Numer. Methods Fluids 82 (5) (2016) 231–260.
[6] L.G. Margolin, W.J. Rider, A rationale for implicit turbulence modelling, Int. J. Numer. Methods Fluids 39 (9) (2002) 821–841.
[7] F.F. Grinstein, L.G. Margolin, W.J. Rider, Implicit Large Eddy Simulation: Computing Turbulent Fluid Dynamics, Cambridge University Press, 2007.
[8] R.C. Moura, S.J. Sherwin, J. Peiró, Modified equation analysis for the discontinuous Galerkin formulation, in: R.M. Kirby, M. Berzins, J.S. Hesthaven (Eds.), Spectral and High Order Methods for Partial Differential Equations, ICOSAHOM 2014, Springer, 2015, pp. 375–383.
[9] R. Moura, G. Mengaldo, J. Peiró, S. Sherwin, An LES setting for DG-based implicit LES with insights on dissipation and robustness, in: Spectral and High Order Methods for Partial Differential Equations, ICOSAHOM 2016, Springer, 2017 (under preparation).
[10] R.C. Moura, S.J. Sherwin, J. Peiró, Linear dispersion–diffusion analysis and its application to under-resolved turbulence simulations using discontinuous Galerkin spectral/*hp* methods, J. Comput. Phys. 298 (2015) 695–710.
[11] G.J. Gassner, A.D. Beck, On the accuracy of high-order discretizations for underresolved turbulence simulations, Theor. Comput. Fluid Dyn. 27 (3–4) (2013) 221–237.
[12] W.J.T. Bos, J.P. Bertoglio, Dynamics of spectrally truncated inviscid turbulence, Phys. Fluids 18 (7) (2006) 071701.
[13] Y. Zhou, F.F. Grinstein, A.J. Wachtor, B.M. Haines, Estimating the effective Reynolds number in implicit large-eddy simulation, Phys. Rev. E 89 (1) (2014) 013303.
[14] U. Frisch, Turbulence: the Legacy of A. N. Kolmogorov, Cambridge University Press, 1995.
[15] C.W. Shu, W.S. Don, D. Gottlieb, O. Schilling, L. Jameson, Numerical convergence study of nearly incompressible, inviscid Taylor–Green vortex flow, J. Sci. Comput. 24 (1) (2005) 1–27.
[16] P.E. Vincent, P. Castonguay, A. Jameson, Insights from von Neumann analysis of high-order flux reconstruction schemes, J. Comput. Phys. 230 (22) (2011) 8134–8154.
[17] D. De Grazia, G. Mengaldo, D. Moxey, P.E. Vincent, S.J. Sherwin, Connections between the discontinuous Galerkin method and high-order flux reconstruction schemes, Int. J. Numer. Methods Fluids 75 (12) (2014) 860–877.
[18] G. Mengaldo, D. De Grazia, P.E. Vincent, S.J. Sherwin, On the connections between discontinuous Galerkin and flux reconstruction schemes: extension to curvilinear meshes, J. Sci. Comput. 67 (3) (2016) 1272–1292.
[19] S.B. Pope, Turbulent Flows, Cambridge University Press, 2000.
[20] A.D. Beck, D.G. Flad, C. Tonhäuser, G. Gassner, C.D. Munz, On the influence of polynomial de-aliasing on subgrid scale models, Flow Turbul. Combust. 97 (2) (2016) 475–511.
[21] G.I. Taylor, A.E. Green, Mechanism of the production of small eddies from large ones, Proc. R. Soc. Lond. A 158 (895) (1937) 499–521.
[22] D. Drikakis, C. Fureby, F.F. Grinstein, D. Youngs, Simulation of transition and turbulence decay in the Taylor–Green vortex, J. Turbul. 8 (20) (2007).
[23] M.E. Brachet, M. Meneguzzi, A. Vincent, H. Politano, P.L. Sulem, Numerical evidence of smooth self-similar dynamics and possibility of subsequent collapse for three-dimensional ideal flows, Phys. Fluids A, Fluid Dyn. 4 (12) (1992) 2845–2854.
[24] C. Cichowlas, M.-E. Brachet, Evolution of complex singularities in Kida–Pelz and Taylor–Green inviscid flows, Fluid Dyn. Res. 36 (4) (2005) 239–248.
[25] T.Y. Hou, R. Li, Blowup or no blowup? The interplay between theory and numerics, Phys. D, Nonlinear Phenom. 237 (14) (2008) 1937–1944.
[26] M.E. Brachet, D.I. Meiron, S.A. Orszag, B.G. Nickel, R.H. Morf, U. Frisch, Small-scale structure of the Taylor–Green vortex, J. Fluid Mech. 130 (1983) 411–452.
[27] M.E. Brachet, Direct simulation of three-dimensional turbulence in the Taylor–Green vortex, Fluid Dyn. Res. 8 (1) (1991) 1–8.
[28] E.F. Toro, Riemann Solvers and Numerical Methods for Fluid Dynamics, Springer, 1999.
[29] C.D. Cantwell, D. Moxey, A. Comerford, A. Bolis, G. Rocco, G. Mengaldo, D. De Grazia, S. Yakovlev, J. Lombard, D. Ekelschot, B. Jordi, H. Xu, Y. Mohamied, C. Eskilsson, B. Nelson, P. Vos, C. Biotto, R.M. Kirby, S.J. Sherwin, Nektar++: an open-source spectral/*hp* element framework, Comput. Phys. Commun. 192 (2015) 205–219.
[30] L. Diosady, S. Murman, Higher-order methods for compressible turbulent flows using entropy variables, in: Proceedings of the 53rd AIAA Aerospace Sciences Meeting, Kissimmee, USA, 2015, AIAA Paper 2015-0294.
[31] C.C. Wiart, K. Hillewaert, L. Bricteux, G. Winckelmans, Implicit LES of free and wall-bounded turbulent flows based on the discontinuous Galerkin/symmetric interior penalty method, Int. J. Numer. Methods Fluids 78 (6) (2015) 335–354.
[32] G. Mengaldo, D. De Grazia, D. Moxey, P.E. Vincent, S.J. Sherwin, Dealiasing techniques for high-order spectral element methods on regular and irregular grids, J. Comput. Phys. 299 (2015) 56–81.
[33] G. Falkovich, Bottleneck phenomenon in developed turbulence, Phys. Fluids 6 (4) (1994) 1411.
[34] M. Coantic, J. Lasserre, On pre-dissipative 'bumps' and a Reynolds-number-dependent spectral parameterization of turbulence, Eur. J. Mech. B, Fluids 18 (6) (1999) 1027–1047.
[35] A.G. Lamorgese, D.A. Caughey, S.B. Pope, Direct numerical simulation of homogeneous turbulence with hyperviscosity, Phys. Fluids 17 (1) (2005) 015106.
[36] U. Frisch, S. Kurien, R. Pandit, W. Pauls, S.S. Ray, A. Wirth, J.Z. Zhu, Hyperviscosity, Galerkin truncation, and bottlenecks in turbulence, Phys. Rev. Lett. 101 (14) (2008) 144501.
[37] D. Banerjee, S.S. Ray, Transition from dissipative to conservative dynamics in equations of hydrodynamics, Phys. Rev. E 90 (4) (2014) 041001.
[38] Y. Dubief, F. Delcayre, On coherent-vortex identification in turbulence, J. Turbul. 1 (11) (2000).
[39] C. Cichowlas, P. Bonaïti, F. Debbasch, M. Brachet, Effective dissipation and turbulence in spectrally truncated Euler flows, Phys. Rev. Lett. 95 (26) (2005) 264502.
[40] R. Cocle, L. Bricteux, G. Winckelmans, Spectral behavior of various subgrid-scale models in LES at very high Reynolds number, in: J. Meyers, B.J. Geurts, P. Sagaut (Eds.), Quality and Reliability of Large-Eddy Simulations, Springer, 2008, pp. 61–68.
[41] F.Q. Hu, M.Y. Hussaini, P. Rasetarinera, An analysis of the discontinuous Galerkin method for wave propagation problems, J. Comput. Phys. 151 (2) (1999) 921–946.
[42] C.C. de Wiart, K. Hillewaert, M. Duponcheel, G. Winckelmans, Assessment of a discontinuous Galerkin method for the simulation of vortical flows at high Reynolds number, Int. J. Numer. Methods Fluids 74 (7) (2014) 469–493.
[43] M. Minguez, R. Pasquetti, E. Serre, High-order large-eddy simulation of flow over the 'Ahmed body' car model, Phys. Fluids 20 (9) (2008) 095101.
[44] J.-E.W. Lombard, D. Moxey, S.J. Sherwin, J.F.A. Hoessler, S. Dhandapani, M.J. Taylor, Implicit large-eddy simulation of a wingtip vortex, AIAA J. 54 (2) (2016) 506–518.

[45] R.C. Moura, S.J. Sherwin, J. Peiró, Eigensolution analysis of spectral/*hp* continuous Galerkin approximations to advection–diffusion problems: insights into spectral vanishing viscosity, J. Comput. Phys. 307 (2016) 401–422.
[46] J. Malm, P. Schlatter, P.F. Fischer, D.S. Henningson, Stabilization of the spectral element method in convection dominated flows by recovery of skew-symmetry, J. Sci. Comput. 57 (2) (2013) 254–277.
[47] G.J. Gassner, A.R. Winters, D.A. Kopriva, Split form nodal discontinuous Galerkin schemes with summation-by-parts property for the compressible Euler equations, J. Comput. Phys. 327 (2016) 39–66.